Battery Cell Monitoring Unit

Eric C. Danson

Thesis submitted to the faculty of the
Virginia Polytechnic Institute and State University
in partial fulfillment of the requirements for the degree of

Master of Science
in
Electrical Engineering

Dong S. Ha, Chair
Jeffrey S. Walling
Dan M. Sable

April 12, 2023
Blacksburg, Virginia

Keywords: cell monitoring unit (CMU), battery management system (BMS), lithium-ion

Battery Cell Monitoring Unit

Eric C. Danson

(ABSTRACT)

The proposed cell monitoring unit for sensing voltage, current, and temperature in a 12-cell 18650 lithium-ion battery module aims to be low-power, serving as the core of an energy-efficient battery management system and facilitating battery management functions with cell data. Notable features include a switchable voltage divider, a single op-amp differential amplifier and level shifter, and a high-precision composite amplifier. The proposed circuit is implemented on a printed circuit board. Measurement results show that the highest power dissipation under continuous operation is from the current sensing circuit at 6.03 mW under a 4 A string current, followed by the voltage sensing at 2.52 mW for the top cell and the temperature sensing at 34.9 µW. The measured power figures include the power dissipation from the battery cells in addition to the cell monitoring unit. The maximum output error is 68 mV for cell voltages up to 44.4 V, 36 mA for current up to 4 A, and 0.37 °C for temperature up to 73 °C.

Battery Cell Monitoring Unit

Eric C. Danson

(GENERAL AUDIENCE ABSTRACT)

Battery management systems are required in modern rechargeable battery-operated devices to help ensure that the batteries operate within the manufacturer-specified operating range. Otherwise, damage to the batteries or to the device may occur. Battery modules are comprised of smaller energy cells to achieve the specified energy capacity and power output. At the core of a battery management system is a battery cell monitoring unit that interfaces the management system with the battery module by providing data about each of the battery cells, including voltage, current, and temperature. To help minimize the power dissipation of battery-powered devices and prolong the battery life, the power consumed by the battery management system should be small. This project aims to detail the design and results of a low-power cell monitoring unit as the core component of energy-efficient battery management systems. The proposed circuit is designed for a 12-cell lithium-ion battery module and implemented on a printed circuit board. The maximum measured power dissipation under continuous operation is 6.03 mW for the current sensing circuit, followed by the voltage sensing circuit at 2.52 mW and the temperature sensing circuit at 34.9 µW.

Acknowledgments

Many thanks to my advisor, Dr. Dong Ha, for his guidance. I would also like to thank Dr. Dan Sable for his expertise and his excellent class on electronic circuit design. Thank you to all of my committee members for the opportunities and for your continued support during my time at Virginia Tech.

Contents

List of Figures

List of Tables

List of Abbreviations

ADC analog-to-digital converter

BMS battery management system

CMRR common-mode rejection ratio

CMU cell monitoring unit

DUT device under test

IC integrated circuit

NTC negative temperature coefficient

PCB printed circuit board

RMS root mean square

RTD resistance temperature detector

Chapter 1

Introduction

1.1 Motivation

Future trends in battery management system (BMS) technology focus on techniques for state estimation, active cell balancing, and optimal charging to maximize battery safety, efficiency, and lifespan [1–6]. For example, the state of health reflects the available discharge capacity relative to the rated capacity and is an important metric for knowing when to replace aging batteries or to identify the onset of battery failure [7]. Since the BMS functions rely on battery cell monitoring, this project aims to increase the energy efficiency of battery-powered systems through a low-power cell monitoring unit (CMU). Considering the large number of battery cells in electric vehicles, reducing the power dissipation of each CMU as well as improving the sensed value accuracy is important. However, the power dissipation of CMUs has been neglected so far, and, to my knowledge, there are no recent papers published in open literature regarding low-power design of CMUs. A side effect can be reducing the cost of such systems by using low supply voltages and avoiding the need for specialized high-voltage components to interface with the battery module. A low-power CMU has the potential to be self-contained, being self-powered by energy harvesting techniques and able to operate independently of the battery module being monitored.

1.2 Outline

Chapter 2 reviews lithium-ion batteries and cell monitoring units. Chapter 3 presents the proposed circuit with optimizations for low power dissipation. Chapter 4 shows the results, including accuracy and power measurements. Chapter 5 concludes the thesis and proposes possible improvements.

Chapter 2

Preliminaries

2.1 Lithium-Ion Battery

Lithium-ion (Li-ion) batteries have high energy and power density, low weight, low internal impedance and self-discharge resulting in high efficiency, and a long cycle life compared to lead-acid and nickel-metal hydride compositions [8, 9]. Cylindrical 18650 Li-ion cells, where 18650 refers to the physical 18 mm diameter and 65 mm length, have a typical 2.5–4.2 V operating range and a nominal 3.6–3.7 V rating [10]. Battery modules are organized as parallel strings of series cells to provide the required voltage, current capability, and energy capacity for a given application.

2.2 Cell Monitoring Unit

The CMU is the key building block of a BMS. A CMU usually monitors cell voltages, currents, and temperatures within a battery module. The CMU provides data to detect under/overvoltage, overcurrent, and under/overtemperature conditions that could damage the battery. The cell data can also be used to calculate the overall battery state of charge and health in a BMS [9–11].

Chapter 3

Proposed Cell Monitoring Circuit

The proposed CMU (Fig. 3.1) is developed for a single string of twelve 18650 Li-ion cells to demonstrate the circuit's capability. Additional units can be added for battery modules containing parallel strings for higher cell counts. Figure 3.2 shows an example implementation with three CMUs for 36 cells. The proposed CMU is not specific to any particular manufacturer's battery series; the circuit depends only on the battery's operating voltage, current, and temperature range. The proposed architecture is flexible and could be adapted to other battery types by adjusting the component parameters.

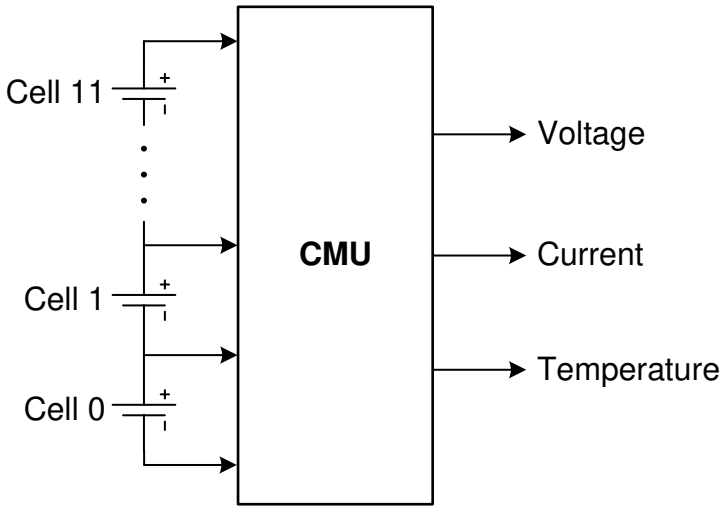

Figure 3.1: System overview block diagram.

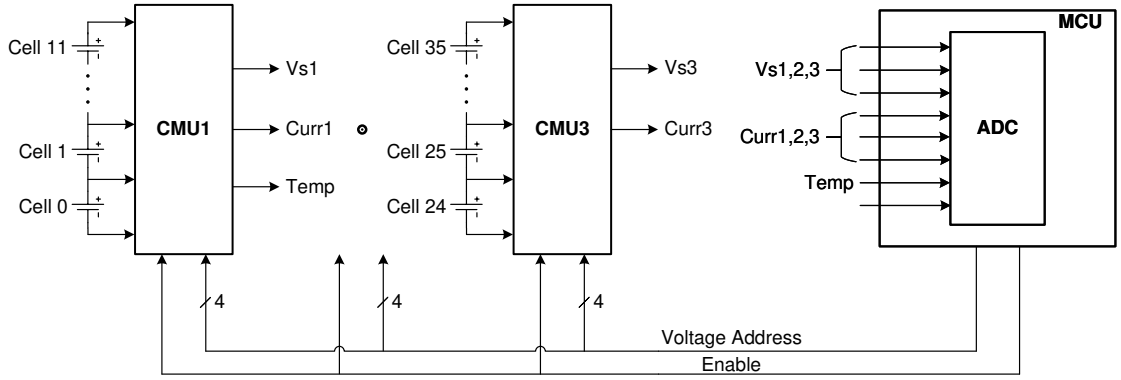

Figure 3.2: System overview block diagram example for 36 cells.

3.1 Voltage Sensing

Figure 3.3 shows a block diagram overview for voltage sensing. A sequential approach is chosen in which only one cell voltage is measured at a time rather than a parallel approach where multiple cell voltages are measured simultaneously. Thus, only one cell needs to be connected to the sensing circuitry, which helps minimize the energy drawn from the battery module during measurement. A sequential approach also requires fewer active components, as opposed to an amplifier for each individual cell in the parallel approach, thus reducing the overall power dissipation and limiting potential sources of measurement error variance between cells.

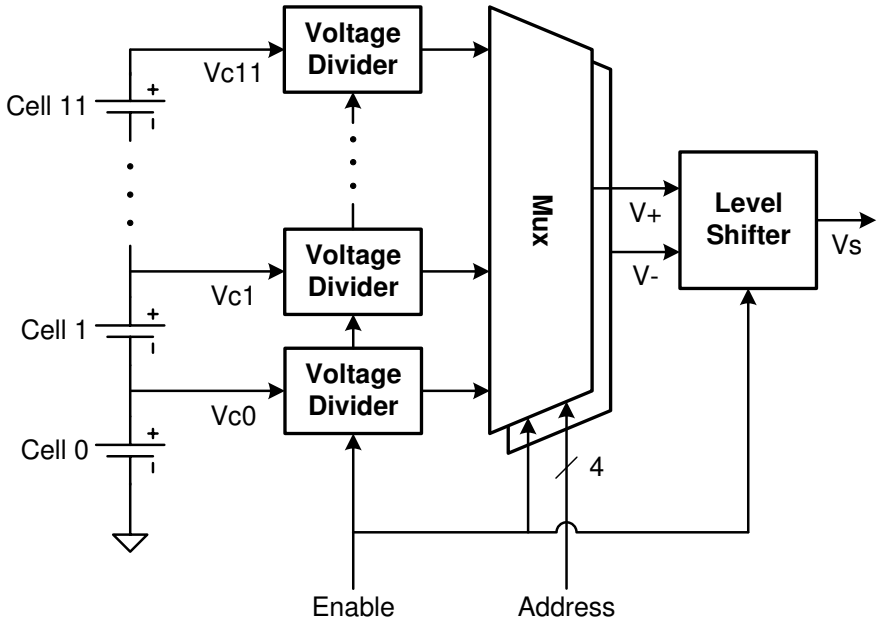

Figure 3.3: Voltage sensing block diagram.

3.1.1 Cell Voltage Divider

The power dissipation is proportional to the circuit's supply voltage when considering that analog integrated circuits (ICs) such as op-amps are biased by current sources. Common components available on the market also often have maximum voltage ratings less than the battery module voltage. By scaling down the cell voltages with a voltage divider, the resulting signal is compatible with the low supply voltage desired for the active sensing components. A voltage divider with enable (Fig. 3.4) is configured in a 10:1 ratio with the component values in Table 3.1 to scale the maximum battery module voltage, seen at the top cell, from 50 V to 5 V. The V_{switch} signal allows each cell to be connected or disconnected from the measurement circuitry. Q1 controls the current through R_1 and R_2 and consequently the gate voltage of Q2 to control the current through R_3 and R_4. The output is

$$V_{div} = \frac{R_4}{R_3 + R_4} V_{cell} = 0.1 V_{cell} \tag{3.1}$$

when V_{switch} is asserted and zero otherwise. The voltage divider created by R_1 and R_2 with the output

$$V_{g2} = \frac{R_2}{R_1 + R_2} V_{cell} = 0.2703 V_{cell} \tag{3.2}$$

when V_{switch} is asserted limits the maximum source-to-gate voltage seen by Q2 to a safe value to avoid damaging the transistor. Q1 and Q2 are chosen to have a sufficiently large maximum drain-to-source voltage rating to withstand the battery module voltage. Q1 and Q2 are also selected to have a low threshold voltage to be able to be switched from a typical 3.3 V microcontroller's digital I/O pins.

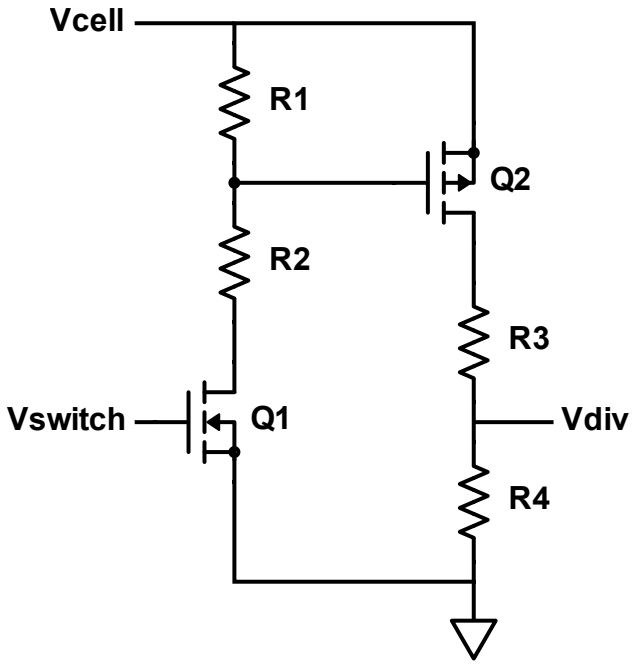

Figure 3.4: Voltage sensing divider schematic.

Table 3.1: Voltage Sensing Divider Component Values

Component	**Value**
$R_1,\ R_3$	2.7 MΩ
R_2	1 MΩ
R_4	300 kΩ
Q1	Infineon BSS123N H6237
Q2	Infineon BSP316P H6327

3.1.2 Differential Amplifier and Level Shifter

A level shifter can effectively move the cell's minimum voltage to near zero (Fig. 3.5), which reduces the maximum voltage seen by an analog-to-digital converter (ADC) and improves the maximum attainable resolution because the ADC reference voltage can be reduced to the difference between the minimum and maximum cell voltages. The maximum theoretical resolution for an N-bit ADC is

$$(\Delta V)_{min} = \frac{V_{ref}}{2^N}. \tag{3.3}$$

Reducing V_{ref} from 3.3 V to 1.8 V, for example, results in a 45.5% higher maximum theoretical resolution, although the effective resolution is limited by noise and bandwidth [12].

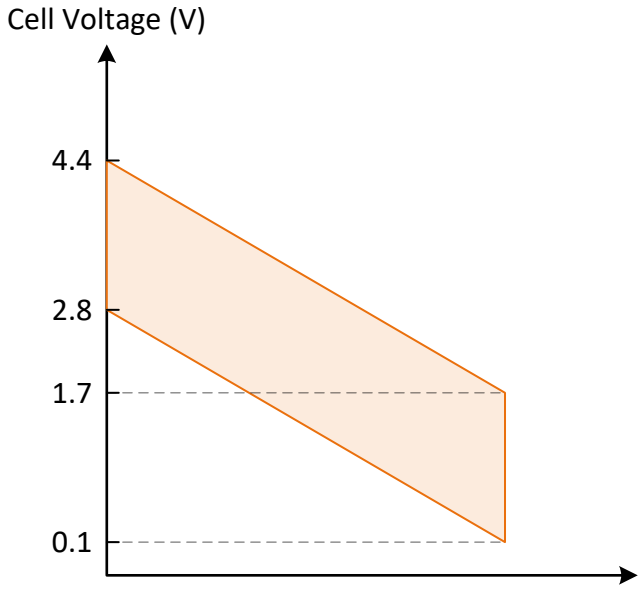

Figure 3.5: Level shifter operation.

The scaled cell voltages are multiplexed with differential outputs from two analog 16-to-1 multiplexers into a differential amplifier and level shifter comprised of a single op-amp (Fig. 3.6) with the component values in Table 3.2. The amplifier is configured for 10× gain, the inverse of the cell voltage divider, to scale the cell voltages back to the original level and maintain the dynamic range. For cell N, the differential amplifier calculates the cell voltage, $V_N - V_{N-1}$, while the level shifter simultaneously shifts the cell voltage from 2.8–4.4 V down to 0.1–1.7 V (Fig. 3.5). The 0.1 V offset is to account for op-amps not being able to output exactly 0 V from a single supply. The total output is

$$\begin{aligned} V_{out} &= \left(1 + \frac{R_1}{R_2||R_3}\right) \frac{R_5}{R_4 + R_5} v_2 - \frac{R_1}{R_3} v_1 - \frac{R_1}{R_2} V_{ref} \\ &= 10\,(v_2 - v_1) - 2.7. \end{aligned} \tag{3.4}$$

A dedicated Analog Devices LT6656-1.25 voltage reference for the level shifter provides a

stable V_{ref} input as opposed to using the supply voltage line which can fluctuate under load. The circuit is powered from a single 5 V supply to accommodate a 50 V battery module but could support a higher battery module voltage with a different cell divider ratio.

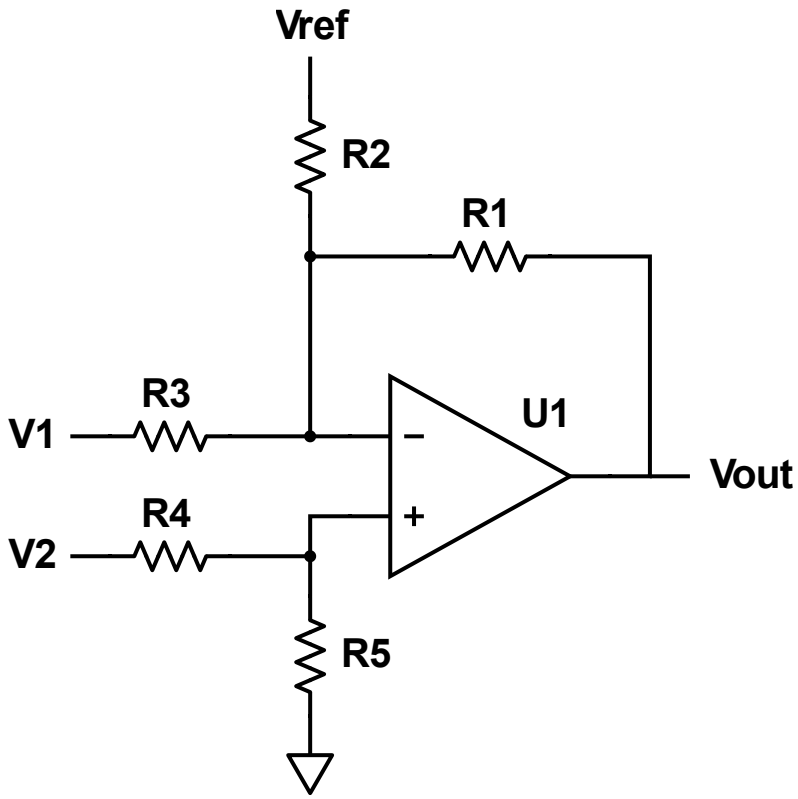

Figure 3.6: Voltage sensing differential amplifier and level shifter schematic.

Table 3.2: Voltage Sensing Differential Amplifier and Level Shifter Component Values

Component	**Value**
R_1	$1\,\mathrm{M}\Omega$
R_2	$463\,\mathrm{k}\Omega$
$R_3,\ R_4$	$100\,\mathrm{k}\Omega$
R_5	$316.5\,\mathrm{k}\Omega$
V_{ref}	$1.25\,\mathrm{V}$
U1	Maxim MAX9917

Buffers are added at the multiplexer outputs (Fig. 3.7) in the prototype implementation to isolate the level shifter from the preceding stages and maintain the desired gain by mitigating loading effects. An instrumentation amplifier serves the same purpose in a single package but currently has limited options available in the low-power category. The multiplexers are the Maxim MAX396, and the buffers are the Maxim MAX9917. All the components are chosen for a low supply current and have an enable feature to turn off the device and save power when the voltage is not being sensed.

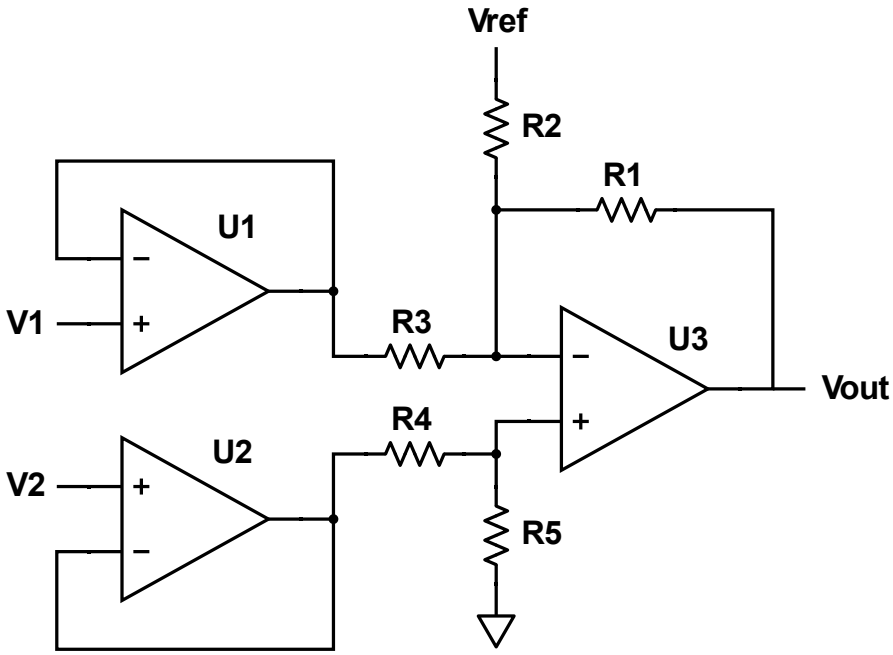

Figure 3.7: Voltage sensing differential amplifier and level shifter schematic with buffers.

Figure 3.8 shows the simulated frequency response of the proposed voltage sensing circuit in LTspice. The 6.45 kHz bandwidth is limited by the multiplexer output capacitance in parallel with the voltage divider resistance creating a pole in the low kHz range. The bandwidth could be increased by using smaller resistors at the cost of higher power dissipation or by using multiplexers with a smaller output capacitance. Simulation results show little dependence of the frequency response on temperature between −40–150 °C (Fig. 3.9).

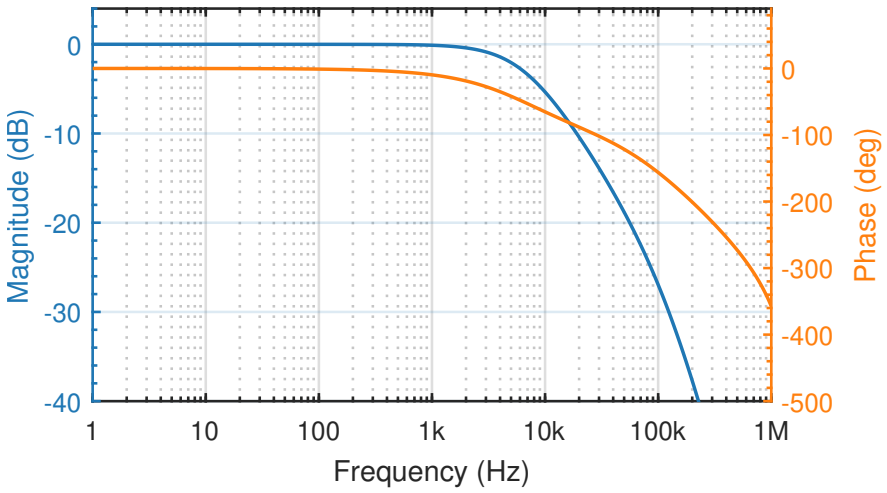

Figure 3.8: Simulated voltage sensing frequency response.

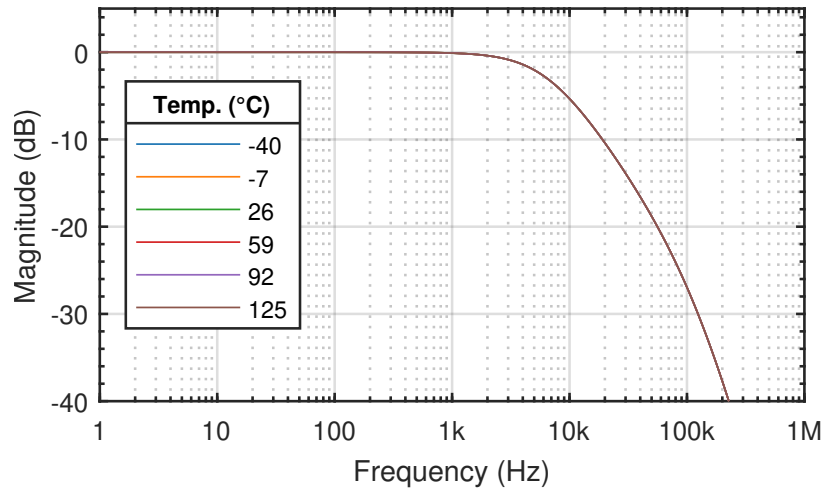

(a)

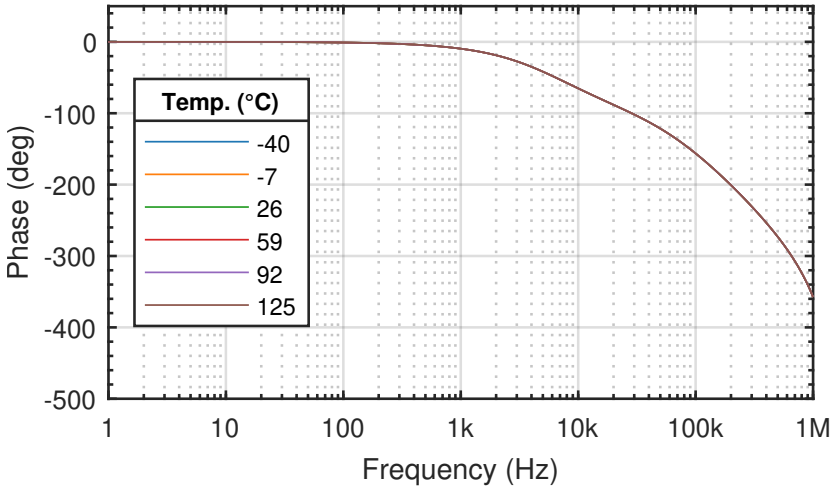

(b)

Figure 3.9: Simulated voltage sensing (a) magnitude and (b) phase over temperature.

3.2 Current Sensing

The power dissipated in a resistor

$$P_R = I^2 R \tag{3.5}$$

is proportional to the current squared, so a current sense resistor can dissipate significant power at high currents. However, low sense resistor values require greater amplification

and careful attention to the signal path to maintain accuracy in the presence of non-ideal component characteristics including offset voltage, leakage current, and Johnson-Nyquist noise. Components with very low offset voltage, bias current, and noise trade power for precision, so reducing the power dissipated by the sense resistor increases the power in other parts of the circuit, but the overall power saved is much greater than the extra power needed for amplification. For example, a 3 A current will dissipate 450 mW in a 50 mΩ resistor and 0.45 mW in a 50 µΩ resistor, while op-amps consume power on the order of a few mW or less.

Low sense resistor values in the µΩ range mean that parasitic resistance in the resistor contacts or wires may contribute considerably to the current sensing output error at high currents. High currents will produce a voltage drop across the parasitic resistance that would be included in the measurement for two-terminal resistors. Four-terminal current sense resistors (Fig. 3.10) instead provide two additional terminals directly across the primary resistive material, and ideally no current flows through the sense terminals, avoiding potential voltage drops at high currents that would be amplified by the measurement device.

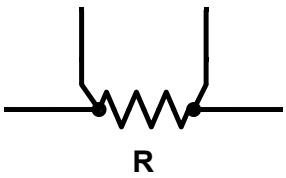

Figure 3.10: Four-terminal current sense resistor.

3.2.1 Composite Amplifier

The current is sensed with a differential DC-stabilized composite amplifier (Fig. 3.11) based on [13] with the component values in Table 3.3. The amplifier is configured for -10000×

or 80 dB gain and connected across a low-side 50 µΩ four-terminal sense resistor between the battery module's negative terminal and ground [14]. The gain is sufficient to amplify signals in the µV range up to the low V range. Unlike the voltage sensing circuit in which each cell voltage may vary, all the cells in the battery module string have the same current, so the current sensing circuit has only one output to be measured. U1 is configured as an integrator to provide DC stability and gain at low frequencies, while U2 as an inverting amplifier provides wide bandwidth and gain at high frequencies. The integrator does not require a parallel resistor in the feedback path for stability, as the integrator is contained within the feedback loop of the composite amplifier and self-regulates. As the input to the integrator increases, the integrator output becomes more negative, thus reducing the input to a stable value. The integrator's high DC gain benefits accuracy by mitigating any effect on the composite amplifier output due to U2's offset voltage. The circuit's effective offset voltage is determined by U1. The lowest power op-amps with wide bandwidth for U2 currently available on the market utilize PNP transistor input stages with non-negligible bias current in the hundreds of nA, so Q1 and Q2 form a current mirror to sink U2's bias current away from R_1 where a small voltage drop would be amplified and create an offset at the output. Both U1 and U2 are chosen for a low supply current and have an enable feature to turn off the device and save power when the current is not being sensed.

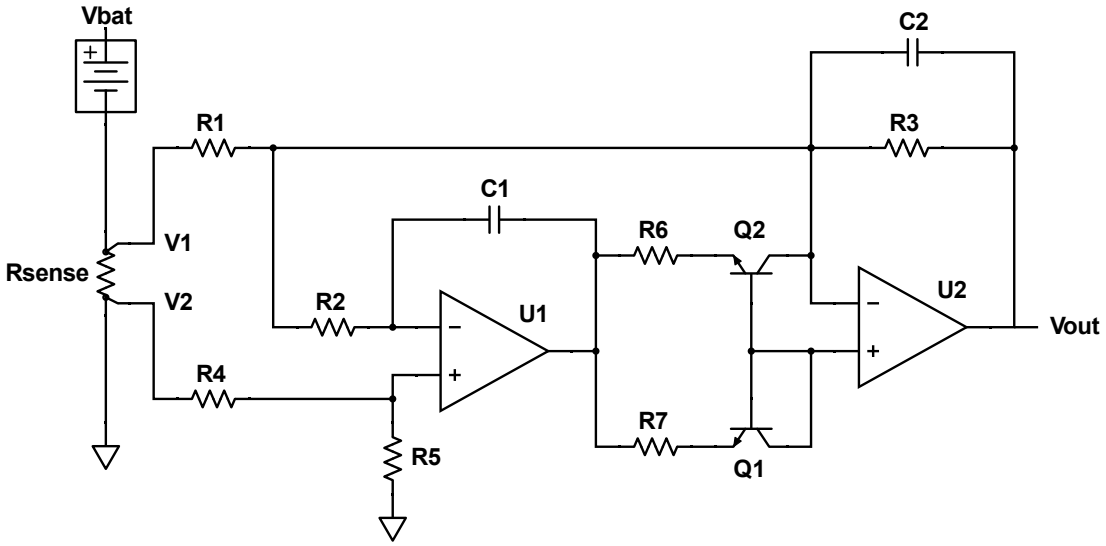

Figure 3.11: Current sensing schematic.

Table 3.3: Current Sensing Component Values

Component	**Value**
R_{sense}	50 µΩ
$R_1,\ R_4$	10 Ω
$R_2,\ R_6,\ R_7$	1 kΩ
$R_3,\ R_5$	100 kΩ
$C_1,\ C_2$	100 pF
Q1, Q2	onsemi MMBT5089
U1	Maxim MAX4238
U2	Analog Devices ADA4805-1

The current through the sense resistor is obtained as

$$I_{sense} = \frac{V_{sense}}{R_{sense}} = \frac{V_{out}}{-10 \times 10^3} \cdot \frac{1}{50 \times 10^{-6}} = -\frac{V_{out}}{0.5} \tag{3.6}$$

with the sensed current range determined by the supply voltage. A single supply allows only for unidirectional current sensing, but a dual supply has the best accuracy for both uni- and bidirectional sensing with the circuit's ability to output 0 V for a 0 A sense current. Therefore, a ± 2.5 V supply is chosen for the amplifier. A high-side sense resistor could also be used and has the advantage of being able to sense short circuit conditions, but high-side current sensing poses the challenge of interfacing with the full common-mode battery module voltage [14]. The small low-side resistor provides a negligible voltage drop between the battery module's negative terminal and ground, so any load connected will effectively see the full battery module voltage.

The composite amplifier's overall transfer function can be found by superposition. Combining the outputs due to each input, the total output is

$$v_o = v_{o1} + v_{o2} \tag{3.7}$$

where

$$v_{o1} = -\frac{R_3}{R_1}\left(\frac{1}{1 + sR_3C_2}\right) v_1 = -10 \times 10^3 \left(\frac{1}{1 + \frac{s}{100 \times 10^3}}\right) v_1 \tag{3.8}$$

is the output due to v_1, and

$$v_{o2} = \frac{R_5\,(R_1 + R_3)}{R_1\,(R_4 + R_5)}\left[\frac{1 + s\,(R_1 \| R_3)\,C_2}{1 + sR_3C_2}\right] v_2 = 10 \times 10^3 \left(\frac{1 + \frac{s}{1 \times 10^9}}{1 + \frac{s}{100 \times 10^3}}\right) v_2 \tag{3.9}$$

is the output due to v_2. Based on the transfer function analysis, the composite amplifier circuit has identical gain to that of the standard differential amplifier configuration in Fig. 3.12

with

$$v_{o1} = -\frac{R_2}{R_1} v_1 \tag{3.10}$$

and

$$v_{o2} = \left(1 + \frac{R_2}{R_1}\right) \frac{R_4}{R_3 + R_4} v_2 = \frac{R_4 \left(R_1 + R_2\right)}{R_1 \left(R_3 + R_4\right)} v_2. \tag{3.11}$$

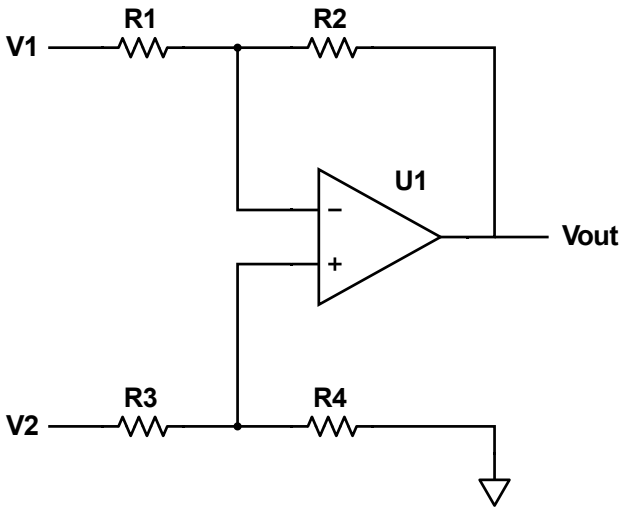

Figure 3.12: Standard differential amplifier schematic.

Figure 3.13 shows the simulated frequency response of the proposed current sensing circuit in LTspice. R_3 and C_2 in Fig. 3.11 create a pole at 15.92 kHz to limit the bandwidth and minimize the error due to high-frequency noise. The usable bandwidth is approximately 1.592 kHz before the magnitude begins to decrease, but an input-to-output delay occurs after approximately 100 Hz where the phase begins to decrease. Simulation results show little dependence of the frequency response on temperature between −40–150 °C (Fig. 3.14).

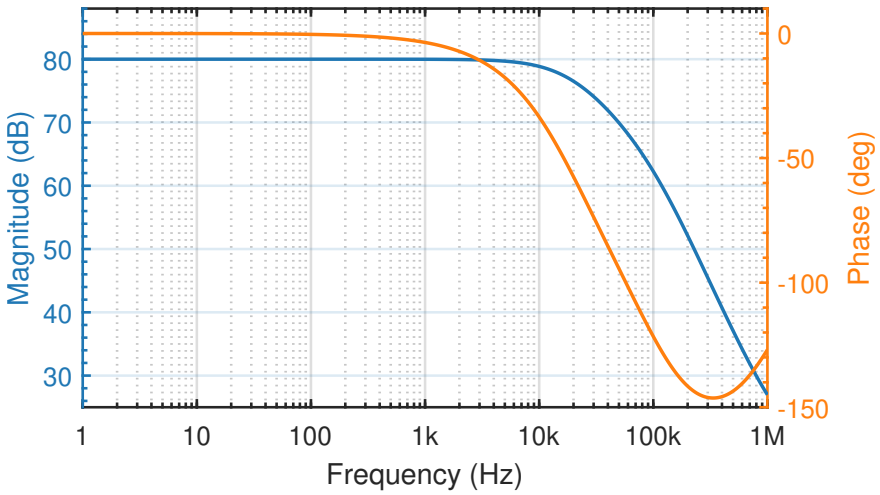

Figure 3.13: Simulated current sensing frequency response.

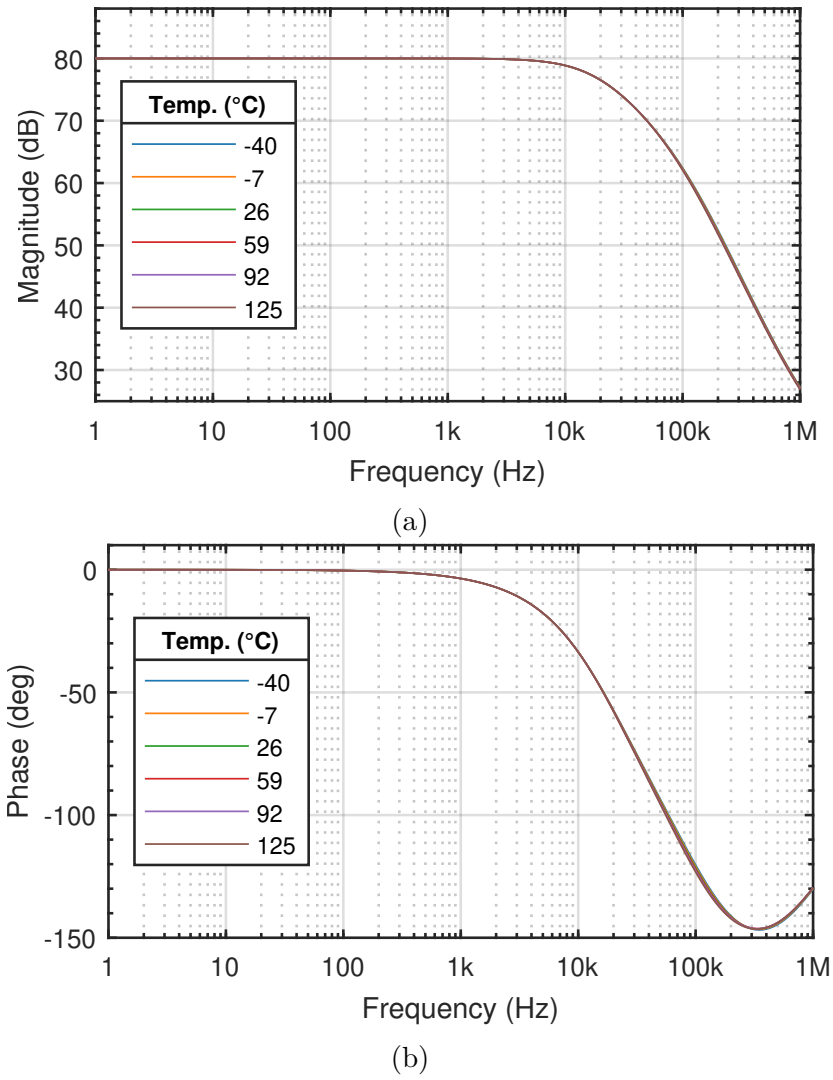

Figure 3.14: Simulated current sensing (a) magnitude and (b) phase over temperature.

Figure 3.15 shows the simulated common-mode rejection ratio (CMRR), defined as the ratio of the differential-mode gain to the common-mode gain

$$CMRR = \left| \frac{A_{dm}}{A_{cm}} \right|. \tag{3.12}$$

The CMRR is 140 dB or 10×10^6 at 0.1 Hz, so common-mode DC values are significantly rejected. The curve corresponds to the integrator gain since the composite amplifier's positive

input goes to the integrator. Thus, increasing the integrator gain improves the circuit's DC accuracy and is limited by the chosen device's open-loop gain.

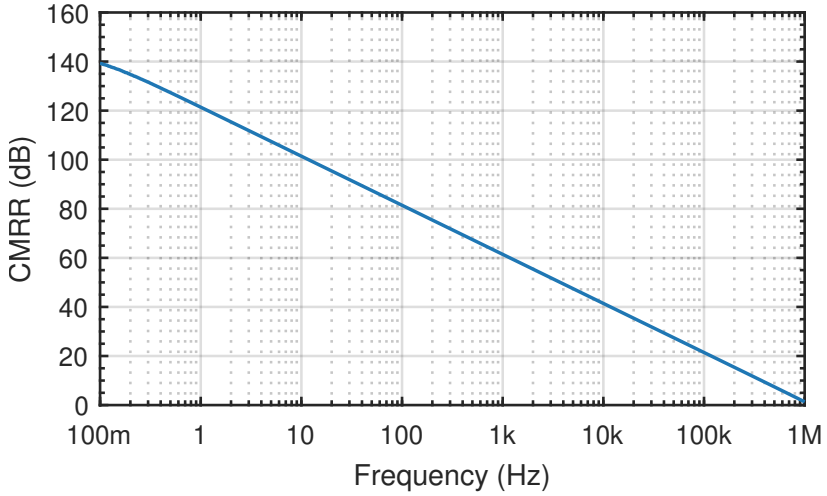

Figure 3.15: Simulated current sensing CMRR.

Figure 3.16 shows the simulated noise density at the output from 0.1 Hz to 100 kHz. The noise increases with temperature up to 286.4 µV root mean square (RMS) total at 125 °C (Table 3.4), which is much less than the $0.5\,\mathrm{V}\cdot\mathrm{A}^{-1}$ amplifier output from the current sense resistor.

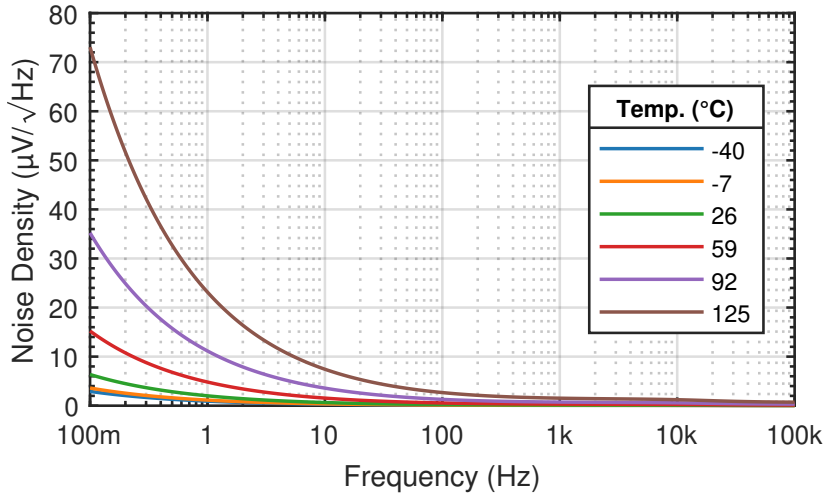

Figure 3.16: Simulated current sensing noise density over temperature.

Table 3.4: Current Sensing Total RMS Noise From 0.1 Hz to 100 kHz

Temp. (°C)	**Total RMS Noise (µV)**
-40	13.38
-7	14.95
26	23.67
59	56.17
92	133.7
125	286.4

3.3 Temperature Sensing

Resistance temperature detectors (RTDs), thermistors, and thermocouples are the three main types of temperature sensors [15]. Thermistors are available with large resistance and have high sensitivity, exhibiting relatively large changes in resistance per unit temperature at the cost of a nonlinear response compared to a typical 100 Ω RTD. Figure 3.17 shows an example negative temperature coefficient (NTC) thermistor characteristic curve in which the resistance decreases exponentially with temperature. The high resistance and sensitivity are ideal for minimizing the power dissipation while maximizing the sensing accuracy at low supply voltages. The third sensor type, the thermocouple, has comparatively low sensitivity but higher maximum operating temperatures.

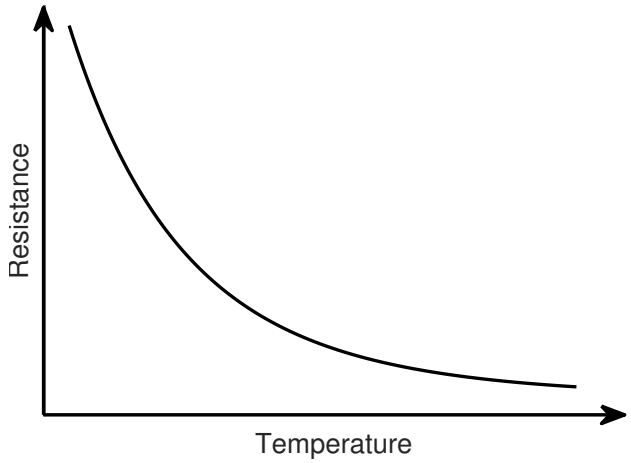

Figure 3.17: NTC thermistor characteristic curve.

3.3.1 Thermistor Divider

A thermistor in series with a bias resistor (Fig. 3.18) with the component values in Table 3.5 form a voltage divider to sense temperature [15]. The cells in the battery module, being in close proximity to one another, are likely to have a small temperature variance, so only one temperature sensing circuit is included to monitor all the cells. A small reference voltage and large resistance are desired to minimize power, so the Analog Devices LT6656-1.25 is chosen as the reference along with an NTC thermistor, the TE Connectivity GA100K6A1IA. The bias resistor R_B is assumed to be temperature insensitive. The bias resistor value is chosen to be equal to the nominal thermistor value so that the output voltage is half the reference voltage at 25 °C, allowing equal voltage swing in either direction for cold and hot temperatures. No enable/disable function is included in the temperature sensing circuit because any reduction in power dissipation would be negligible when considering the additional components required.

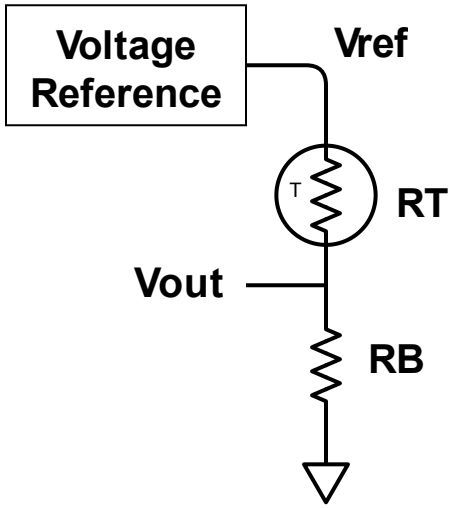

Figure 3.18: Temperature sensing schematic.

Table 3.5: Temperature Sensing Component Values

Component	**Value**
$R_T,\ R_B$	$100\,\mathrm{k}\Omega$
V_{ref}	$1.25\,\mathrm{V}$

Chapter 4

Results and Discussion

4.1 Measurement Setup

Figure 4.1 shows the hand-soldered two-layer printed circuit board (PCB) prototype implementation with physical dimensions 4.9 in. × 2.9 in. The power dissipation was too small to be accurately measured from a bench DC power supply. Instead, the power for each subcircuit was found by measuring the voltage drop across a sense resistor placed between the voltage supply and the circuit under test (Fig. 4.2) and using the formula

$$P_{DUT} = V_{DUT} I_{DUT} = (V_{supply} - V_{sense}) \frac{V_{sense}}{R_{sense}}. \tag{4.1}$$

The formula subtracts the voltage drop across the sense resistor, retaining only the voltage and current delivered to the device under test (DUT). Measurements were recorded using the Agilent 34401A 6.5 digit multimeter and the Digilent Analog Discovery 2 oscilloscope.

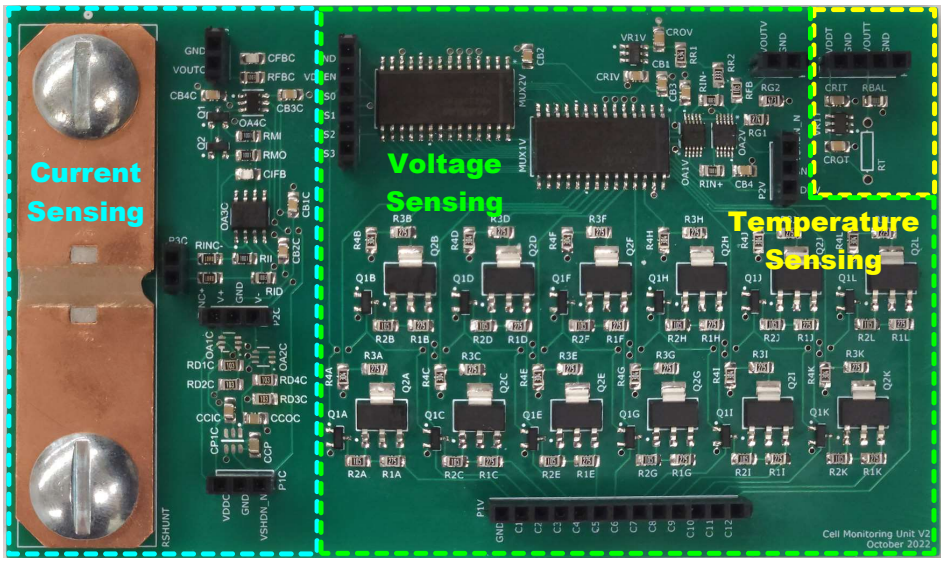

Figure 4.1: PCB prototype implementation.

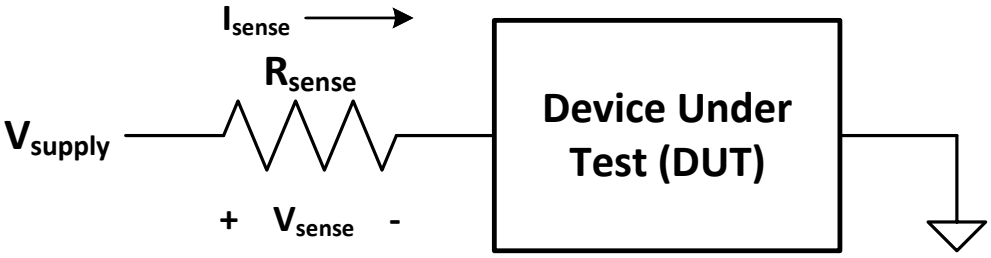

Figure 4.2: Power measurement setup.

4.2 Voltage Sensing

The measured frequency response of the proposed voltage sensing circuit (Fig. 4.3) aligns with the simulated response up to over 100 kHz.

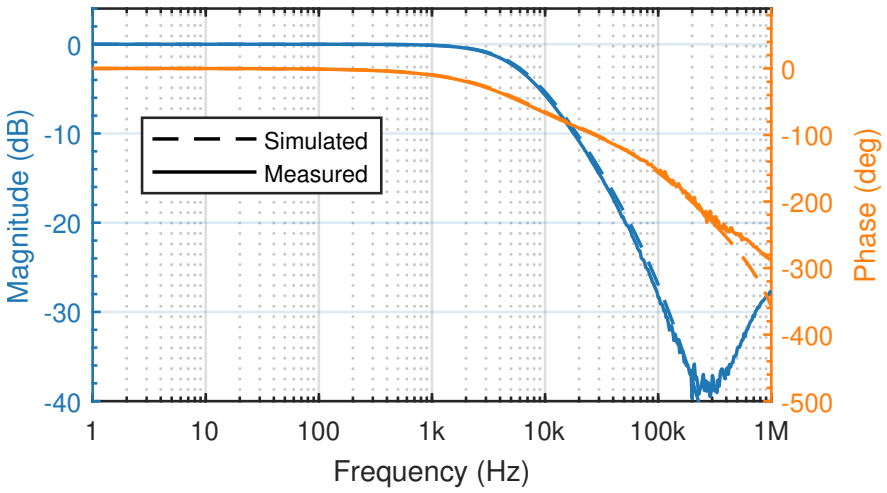

Figure 4.3: Voltage sensing frequency response overlay.

Figures 4.4 and 4.5 show the output waveforms for cells 0 and 11 with sinusoidal inputs. The circuit was measured with sinusoidal inputs to show how the output varies over the full battery cell operating range. The output voltage error increases with the cell number up to a maximum 68 mV for cell 11 (Fig. 4.6) and can be reduced by removing the DC offset using post-processing, centering the error around zero to be within 25 mV over a 1.6 V range.

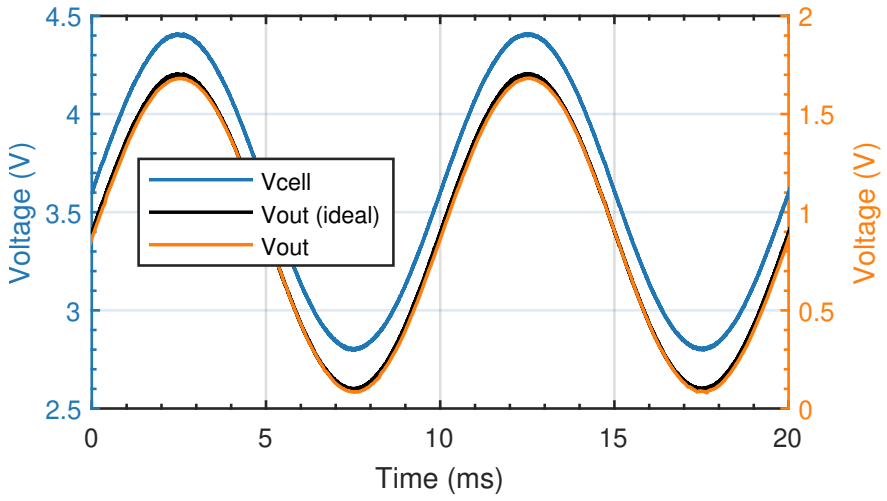

Figure 4.4: Voltage sensing output for cell 0 at 100 Hz.

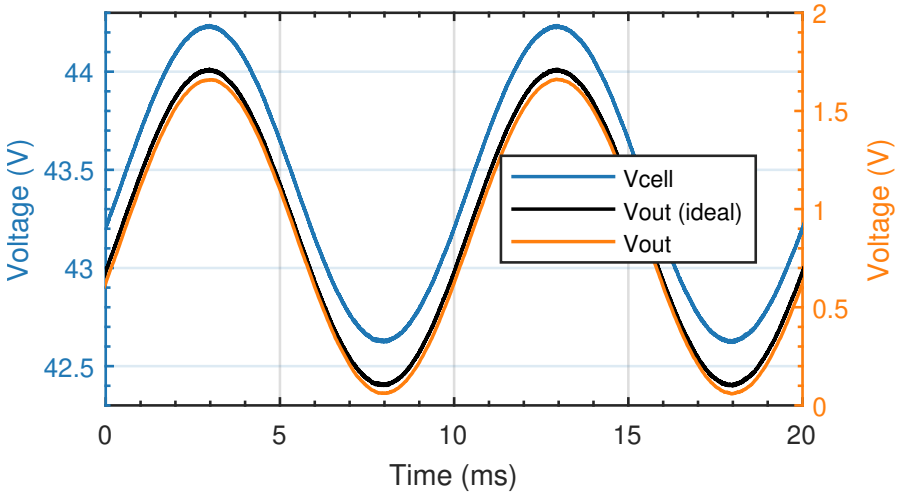

Figure 4.5: Voltage sensing output for cell 11 at 100 Hz.

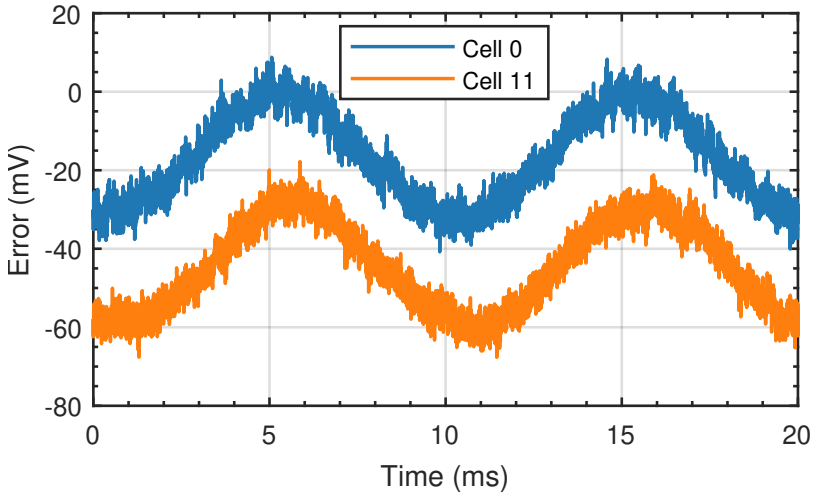

Figure 4.6: Voltage sensing error at 100 Hz.

The average power (Table 4.1) was measured with the cell inputs at the nominal 3.7 V per cell. While the power dissipated in the multiplexers and differential amplifier level shifter from the PCB voltage supply is consistently around one third of a mW, most of the power dissipation is from the cells in the voltage dividers.

Table 4.1: Voltage Sensing Power Dissipation

Cell Position (N)	**Average Power (µW)**			
	PCB	Cell N	Cell N-1	Total
0	302.2	8.15	—	310.4
11	333.2	1187	997.3	2518

4.3 Current Sensing

The measured frequency response of the proposed current sensing circuit (Fig. 4.7) aligns with the simulated response up to 10 kHz, but there is a left-half plane zero in the 100 kHz range that causes the measured magnitude to drop off slower towards 1 MHz. The current sense amplifier still operates as expected in the designed bandwidth and is able to amplify the input voltage -10000× (Fig. 4.8) to within 18 mV of the ideal value (Fig. 4.9). The circuit was measured with a sinusoidal input to show how the output varies over the full operating range. With the 50 µΩ sense resistor, every 0.5 V in the output corresponds to 1 A. The effective current error is then $0.018/0.5 = 36$ mA over a 4 A range.

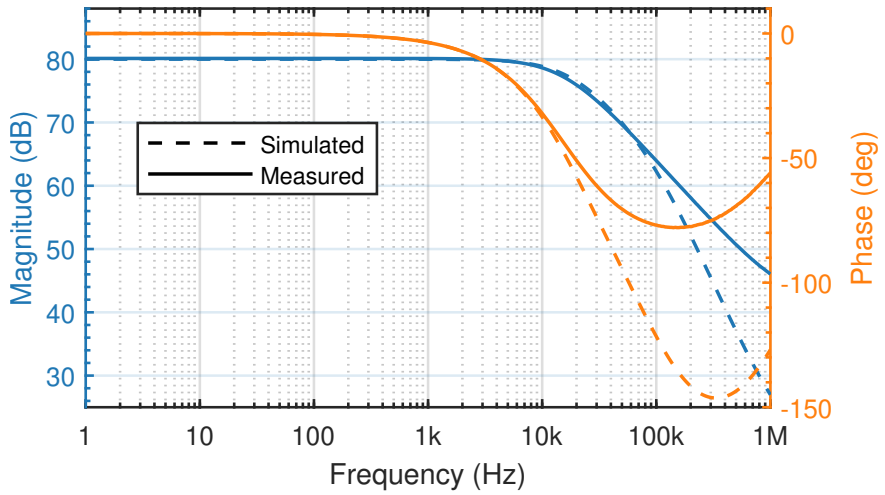

Figure 4.7: Current sensing frequency response overlay.

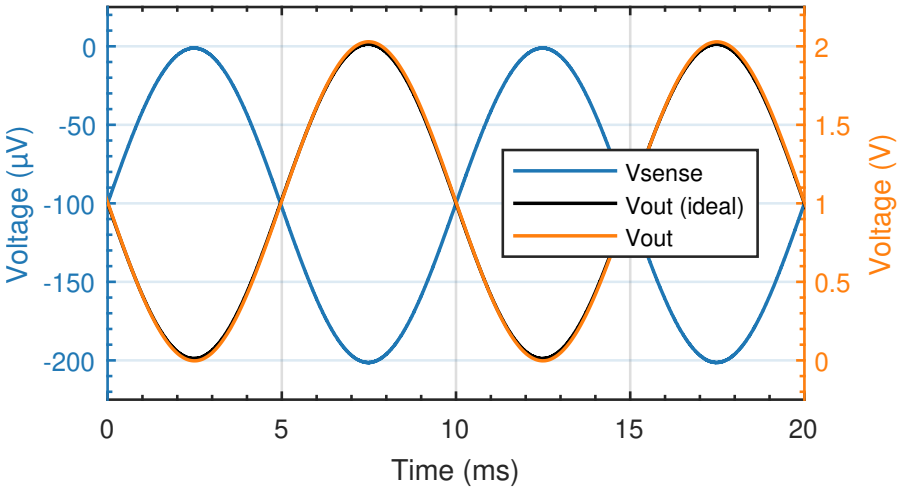

Figure 4.8: Current sensing output at 100 Hz.

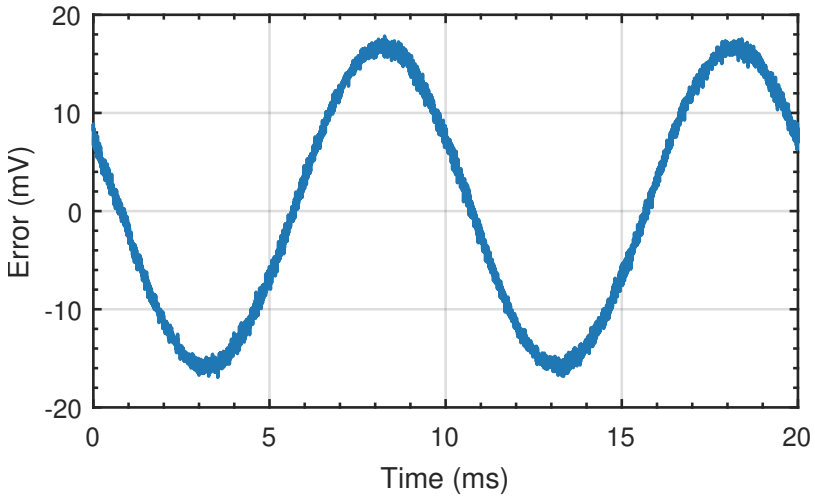

Figure 4.9: Current sensing error at 100 Hz.

The average power (Table 4.2) was measured with the amplifier inputs at constant differential voltages corresponding to 1, 2, 3, and 4 A through the sense resistor. The power dissipated from the PCB voltage supply is consistently around 5.2 mW, and the change in total power is primarily from the current through the sense resistor.

Table 4.2: Current Sensing Power Dissipation

Input (A)	**Average Power (mW)**		
	PCB	Sense Resistor	Total
1	5.247	0.05	5.297
2	5.243	0.2	5.443
3	5.238	0.45	5.688
4	5.231	0.8	6.031

4.4 Temperature Sensing

The output voltage of the proposed temperature sensing circuit was measured inside a Yamato DX302C drying oven from 23–73 °C with a 0.1 mV resolution and recorded manually. The recorded values were then converted to temperature in Kelvin using a Steinhart-Hart model [16] given by

$$T = \left[A + B\ln(R) + C\ln(R)^3\right]^{-1} \tag{4.2}$$

with the coefficients in Table 4.3. The measured temperature (Fig. 4.10) is within 0.37 °C of a BK Precision 710 type K thermometer used as a reference (Fig. 4.11). The positive error may be due to the reference thermometer updating slower than the prototype circuit. The NTC thermistor's nonlinear behavior [15] indicates lower sensitivity at higher temperatures and thus a smaller output voltage change per °C, which explains the increasing error trend when using a fixed 0.1 mV measurement resolution.

Table 4.3: Temperature Sensing Steinhart-Hart Coefficients

Coefficient	**Value**
A	0.8268935666e-3
B	2.088305436e-4
C	0.8052105920e-7

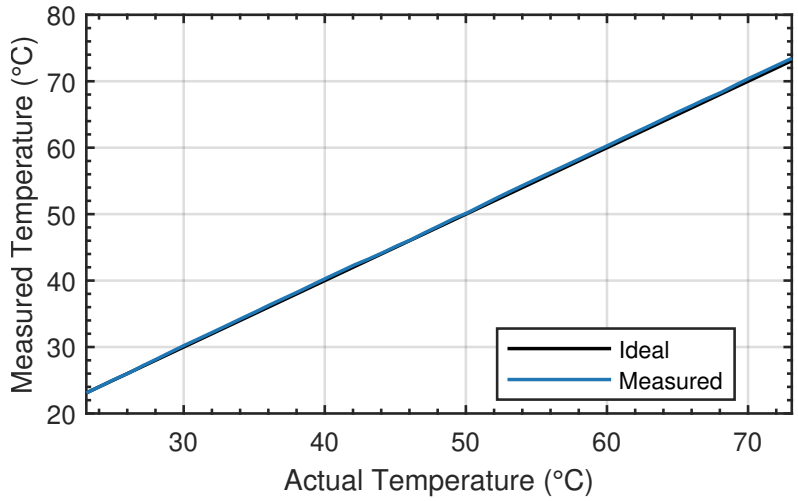

Figure 4.10: Temperature sensing output.

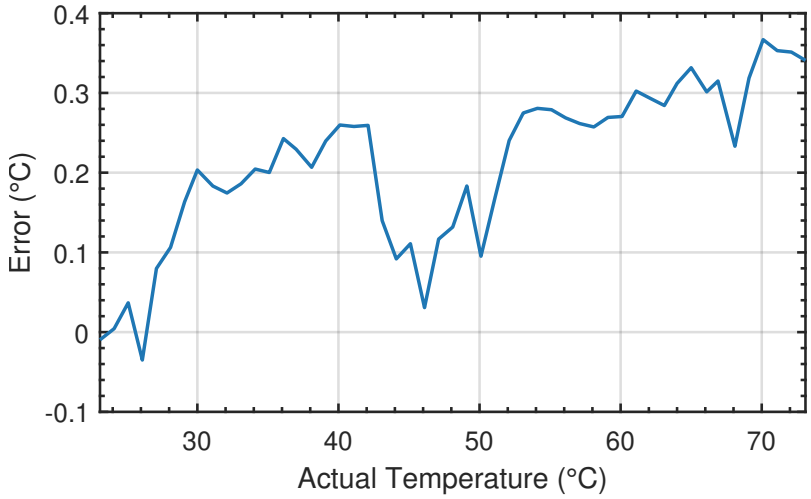

Figure 4.11: Temperature sensing error.

The average power (Table 4.4) was measured at approximately 23 °C and is dominated by the voltage reference. The NTC thermistor's resistance decreases with temperature, so the power dissipation is proportional to temperature, although the overall power dissipation is negligible compared to the voltage and current sensing circuits.

Table 4.4: Temperature Sensing Power Dissipation

Temp. (°C)	**Average Power (µW)**			
	Voltage Ref.	Thermistor	Bias Resistor	Total
23	24.11	5.905	4.888	34.90

4.5 Power Dissipation Comparison

Assuming that the voltage and current circuits are each enabled and being sampled 50% of the time, the proposed CMU dissipates 4.36 mW in total with a 3 A string current (Table 4.5), including the power dissipated by the battery cells. The current sensing circuit dissipates the majority of the power followed by the voltage and temperature sensing circuits. It should be noted that the average power dissipation of the voltage and current sensing circuits will depend on the ADC sampling time and number of samples per second, so the power dissipated by the switchable components will likely be much lower than the total figure shown under normal operating conditions, by a factor of 500 if the circuits are sampled for 1 ms total each second. The current sense resistor cannot be switched off and would then become the major source of power dissipation.

Table 4.5: Power Dissipation Summary

Circuit	**Power Dissipation (mW)**
Voltage sensing	1.26
Current sensing (3 A string current)	3.07
Temperature sensing	0.0349
Total	4.36

Table 4.6 shows the estimated power dissipation of commercial ICs configured for 12 cells in series and a 3 A string current. The estimated power is calculated from the minimum supply voltage, the supply current, and the typical current sense resistor values given in the product datasheets [17–20], usually 1 mΩ at minimum. The proposed CMU reduces the overall power dissipation by at least 60% compared to the Texas Instruments BQ769xx chips. The Linear Technology LTC86xx chips do not support current monitoring. When current monitoring is removed from the proposed CMU, the maximum power dissipation of the CMU would be reduced to 1.29 mW. Then, the power dissipation of the proposed CMU is smaller than that of the Linear Technology ICs by at least 90%.

Table 4.6: Commercial IC Power Dissipation Comparison

Part	**Interface**	**Estimated Power Dissipation (mW)**		
		Voltage Supply	Sense Resistor	Total
BQ769x0	Digital	2.66	9	11.7
BQ76952	Digital	12.7	9	21.7
LTC6803	Digital	34.6	—	34.6
LTC6811	Digital	24.4	—	24.4

Chapter 5

Conclusion and Future Work

A sequential voltage sensing architecture with a switchable voltage divider and a single op-amp differential amplifier and level shifter, a small current sense resistor with a high-precision composite amplifier, and a thermistor temperature sensing circuit achieve low power in a 12-cell lithium-ion battery CMU. The highest power dissipation under continuous operation is from the current sensing circuit at 6.03 mW under a 4 A string current, followed by the voltage sensing at 2.52 mW for the top cell and the temperature sensing at 34.9 µW. The estimated power dissipation of the proposed CMU is smaller than commercial ICs by at least 60%. As a future task, the sensed value accuracy in each circuit may be improved by integrating a machine learning or optimal estimation algorithm to filter the noise in the output and perform automatic circuit calibration in a microcontroller.

Bibliography

[1] Manh-Kien Tran, Satyam Panchal, Tran Dinh Khang, Kirti Panchal, Roydon Fraser, and Michael Fowler. Concept Review of a Cloud-Based Smart Battery Management System for Lithium-Ion Batteries: Feasibility, Logistics, and Functionality. *Batteries*, 8(2):19, February 2022. ISSN 2313-0105. doi:10.3390/batteries8020019.

[2] Haifeng Dai, Bo Jiang, Xiaosong Hu, Xianke Lin, Xuezhe Wei, and Michael Pecht. Advanced battery management strategies for a sustainable energy future: Multilayer design concepts and research trends. *Renewable and Sustainable Energy Reviews*, 138: 110480, March 2021. ISSN 1364-0321. doi:10.1016/j.rser.2020.110480.

[3] M. S. Hossain Lipu, M. A. Hannan, Tahia F. Karim, Aini Hussain, Mohamad Hanif Md Saad, Afida Ayob, Md. Sazal Miah, and T. M. Indra Mahlia. Intelligent algorithms and control strategies for battery management system in electric vehicles: Progress, challenges and future outlook. *Journal of Cleaner Production*, 292:126044, April 2021. ISSN 0959-6526. doi:10.1016/j.jclepro.2021.126044.

[4] M. S. Hossain Lipu, M. A. Hannan, Aini Hussain, Afida Ayob, Mohamad H. M. Saad, Tahia F. Karim, and Dickson N. T. How. Data-driven state of charge estimation of lithium-ion batteries: Algorithms, implementation factors, limitations and future trends. *Journal of Cleaner Production*, 277:124110, December 2020. ISSN 0959-6526. doi:10.1016/j.jclepro.2020.124110.

[5] Xiaosong Hu, Fei Feng, Kailong Liu, Lei Zhang, Jiale Xie, and Bo Liu. State estimation for advanced battery management: Key challenges and future trends. *Re-*

newable and Sustainable Energy Reviews, 114:109334, October 2019. ISSN 1364-0321. doi:10.1016/j.rser.2019.109334.

[6] Qian Lin, Jun Wang, Rui Xiong, Weixiang Shen, and Hongwen He. Towards a smarter battery management system: A critical review on optimal charging methods of lithium ion batteries. *Energy*, 183:220–234, September 2019. ISSN 0360-5442. doi:10.1016/j.energy.2019.06.128.

[7] Huixin Tian, Pengliang Qin, Kun Li, and Zhen Zhao. A review of the state of health for lithium-ion batteries: Research status and suggestions. *Journal of Cleaner Production*, 261:120813, July 2020. ISSN 0959-6526. doi:10.1016/j.jclepro.2020.120813.

[8] Aoxia Chen and Pankaj K. Sen. Advancement in battery technology: A state-of-the-art review. In *2016 IEEE Industry Applications Society Annual Meeting*, pages 1–10, October 2016. doi:10.1109/IAS.2016.7731812.

[9] Molla Shahadat Hossain Lipu, Abdullah Al Mamun, Shaheer Ansari, Md Sazal Miah, Kamrul Hasan, Sheikh T. Meraj, Maher G. M. Abdolrasol, Tuhibur Rahman, Md Hasan Maruf, Mahidur R. Sarker, A. Aljanad, and Nadia M. L. Tan. Battery Management, Key Technologies, Methods, Issues, and Future Trends of Electric Vehicles: A Pathway toward Achieving Sustainable Development Goals. *Batteries*, 8(9):119, September 2022. ISSN 2313-0105. doi:10.3390/batteries8090119.

[10] Roland Dorn, Reiner Schwartz, and Bjoern Steurich. Battery management system. In Reiner Korthauer, editor, *Lithium-Ion Batteries: Basics and Applications*, pages 165–175. Springer, Berlin, Heidelberg, 2018. ISBN 978-3-662-53071-9. doi:10.1007/978-3-662-53071-9_14.

[11] Markus Lelie, Thomas Braun, Marcus Knips, Hannes Nordmann, Florian Ringbeck, Hendrik Zappen, and Dirk Uwe Sauer. Battery Management System Hardware Con-

cepts: An Overview. *Applied Sciences*, 8(4):534, April 2018. ISSN 2076-3417. doi:10.3390/app8040534.

[12] Jeffrey Fredenburg and Michael P. Flynn. ADC trends and impact on SAR ADC architecture and analysis. In *2015 IEEE Custom Integrated Circuits Conference (CICC)*, pages 1–8, September 2015. doi:10.1109/CICC.2015.7338380.

[13] Jim Williams. Composite Amplifiers. Application Note 21, Linear Technology, July 1986.

[14] Mahdi Kashmiri. Current Sensing Techniques: Principles and Readouts. In Andrea Baschirotto, Pieter Harpe, and Kofi A. A. Makinwa, editors, *Next-Generation ADCs, High-Performance Power Management, and Technology Considerations for Advanced Integrated Circuits: Advances in Analog Circuit Design 2019*, pages 143–165. Springer International Publishing, Cham, 2020. ISBN 978-3-030-25267-0. doi:10.1007/978-3-030-25267-0_9.

[15] Ferran Reverter. A Tutorial on Thermal Sensors in the 200th Anniversary of the Seebeck Effect. *IEEE Sensors Journal*, 21(20):22122–22132, October 2021. ISSN 1558-1748. doi:10.1109/JSEN.2021.3105546.

[16] John S. Steinhart and Stanley R. Hart. Calibration curves for thermistors. *Deep Sea Research and Oceanographic Abstracts*, 15(4):497–503, August 1968. ISSN 0011-7471. doi:10.1016/0011-7471(68)90057-0.

[17] BQ769x0 3-Series to 15-Series Cell Battery Monitor Family for Li-Ion and Phosphate Applications. Datasheet, Texas Instruments, March 2022.

[18] BQ76952 3-Series to 16-Series High Accuracy Battery Monitor and Protector for Li-Ion,

Li-Polymer, and LiFePO4 Battery Packs. Datasheet, Texas Instruments, November 2021.

[19] LTC6803-1/LTC6803-3 Multicell Battery Stack Monitor. Datasheet, Linear Technology, 2011.

[20] LTC6811-1/LTC6811-2 12-Cell Battery Stack Monitors. Datasheet, Analog Devices, November 2019.